# Magnetoconvection transient dynamics by numerical simulation*

Sébastien Renaudière de Vaux[1,2,a], Rémi Zamansky[1], Wladimir Bergez[1], Philippe Tordjeman[1], and Jean-François Haquet[2]

[1] Institut de Mécanique des Fluides de Toulouse (IMFT) - Université de Toulouse, CNRS-INPT-UPS, Toulouse, France
[2] CEA, DEN, Cadarache, SMTA/LPMA, F13108 St Paul lez Durance, France

**Abstract.** We investigate the transient and stationary buoyant motion of the Rayleigh-Bénard instability when the fluid layer is subjected to a vertical, steady magnetic field. For Rayleigh number, $Ra$, in the range $10^3$–$10^6$, and Hartmann number, $Ha$, between 0 and 100, we performed three-dimensional direct numerical simulations. To predict the growth rate and the wavelength of the initial regime observed with the numerical simulations, we developed the linear stability analysis beyond marginal stability for this problem. We analyzed the pattern of the flow from linear to nonlinear regime. We observe the evolution of steady state patterns depending on $Ra/Ha^2$ and $Ha$. In addition, in the nonlinear regime, the averaged kinetic energy is found to depend on $Ra$ and to be independent of $Ha$ in the studied range.

## 1 Introduction

The study of magnetoconvection is fundamental in astrophysics, geophysics [1] and condensed matter physics (for instance crystal growth [2]). It is also fundamental in industrial applications, as heat exchanger for nuclear fusion reactors [3], nuclear safety studies [4] or induction heating and stirring [5] in metallurgy. In this study, we focus on the dynamics and pattern motion obtained by numerical simulation of magnetoconvection at low magnetic Reynolds and Prandtl numbers.

When a non-magnetic electrical conducting liquid sustains a constant magnetic field and a temperature gradient, it undergoes the action of the driving buoyancy force, which is counterbalanced by the Lorentz force and the viscous force. These forces are responsible of magnetohydrodynamic (MHD) instabilities, characterized by patterns that govern heat transfer [6,7] and stirring efficiency. The coupling between Navier-Stokes equation and the magnetic induction equation is determined by the value of magnetic Reynolds number $Rm = \mu_0 \sigma \mathcal{U} \mathcal{L}$ where $\mu_0$ is the electromagnetic permeability of vacuum, $\sigma$ is the electrical conductivity of the fluid, and $\mathcal{U}$ and $\mathcal{L}$ are the characteristic velocity and length of the magnetoconvection. The magnetic Reynolds number is related to the hydrodynamic Reynolds number $Re$ by $Rm = RePm$, with $Pm = \mu_0 \sigma \nu$ the magnetic Prandtl number. In many cases, $Pm \sim 10^{-6}$ and consequently $Rm$ is much lower than unity, the magnetic field is weakly perturbed and the advection of the magnetic field is negligible ($O(Rm)$). For incompressible liquids, small height variation and under the Oberbeck-Boussinesq approximation, three other non-dimensional parameters control the flow dynamics: the Prandtl number $Pr = \nu/\kappa$, the Hartmann number $Ha = B_0 \mathcal{L} \sqrt{\sigma/\rho\nu}$ and the Rayleigh number $Ra = g\beta\Delta T \mathcal{L}^3/\nu\kappa$. Here, $\nu$ is the kinematic viscosity, $\kappa$ is the thermal diffusivity, $g$ is the acceleration of gravity, $\beta$ is the thermal expansion coefficient, $\Delta T$ is a characteristic temperature difference, $B_0$ is the magnitude of the magnetic field and $\rho$ is the reference fluid density. $Ra$ expresses the buoyancy to viscous force ratio, and $Ha^2$ is the Lorentz force to viscous force ratio.

Chandrasekhar [1, 8] has developped the linear stability theory for Rayleigh-Bénard magnetoconvection. He found that the convection occurs for $Ra > Ra_c$, where $Ra_c$ the critical Rayleigh number. The marginal stability curve $Ra_c = f(Ha)$ is defined by a zero growth rate $s = 0$ of the infinitely small perturbations. He established that for a magnetic field aligned with gravity, $Ra_c = f(Ha)$, for which $Ra_c \sim \pi^2 Ha^2$ for large $Ha$ values, experimentally validated [9,10]. For horizontal magnetic fields, $Ra_c$ is independent of $Ha$. We define the relative distance to the threshold $\epsilon = (Ra - Ra_c)/Ra_c$. One notes that for strictly positive values of $\epsilon$, the linear stability analysis has never been carried out. Based on a nonlinear stability analysis and for small values of $Ha$ ($Ha < 5$), Busse and Clever [11] showed that stable parallel rolls form for $\epsilon$ smaller than a critical value. For larger values of $\epsilon$, the rolls destabilize by oscillatory convection. This result has been confirmed by Direct Numerical Simulation (DNS), for $Ha < 12$ and

* Supplementary material in the form of four .avi files avail-

e-mail: srenaudi@imft.fr

$\epsilon < 4$ [12]. Spectral simulations have also been performed to characterize chaotic structures for a large range of $\epsilon$, up to $\sim 500$ [13]. Recently Basak *et al.* [14, 15] showed that the energy was proportional to $\epsilon$ for small values of $\epsilon < 1$ and $Ha < 10$ using DNS in a square box. We did not find numerical studies of pattern motion and of dynamics for intermediate values of $(Ha, Ra)$ and $0 < \epsilon < 10$ ($Ha \sim 50$ and $Ra \sim 10^5$). In particular, the transition between the linear and nonlinear dynamics seems to have never been investigated. On the other hand, systematic experiments have been developed for this range of parameters by Yanagisawa *et al.* [16,17]. The pattern motion has been characterized by ultrasonic velocimetry [18] in liquid gallium with and without horizontal magnetic field. They confirmed the structure in rolls, which is destabilized into 3D structures as $Ra$ is increased. Moreover, in the phase diagram $(Ha, Ra)$ they identify five flow regimes for which the patterns were characterized by their wave number. At sufficiently large values of $Ra$ and $Ha$, the different phases characteristic of regime dynamics are separated by isolines of $\tau_{\rm mag}/\tau_{\rm buo} = Ra/Ha^2$, where $\tau_{\rm mag} = \rho/\sigma B_0^2$ and $\tau_{\rm buo} = \kappa/g\beta\Delta T h$.

In this paper, we studied by DNS the destabilization of an electrically conducting fluid, subject to a magnetic field and to a temperature gradient, both aligned with gravity. Following the results from Chandrasekhar [1, 8], we focus on the application of a vertical magnetic field to study the effects of $Ha$ on the marginal stability. A rectangular Rayleigh-Bénard cell is considered with an aspect ratio of 10 and periodic boundary conditions perpendicular to the vertical axis. This study was performed for $Ha = 0$, 9, 18 and 36, and for $10^4 < Ra < 1.5 \cdot 10^5$, with $0 < \epsilon < 100$. In parallel, we realized the linear stability analysis for a large range of $(Ha, Ra)$ values and confronted the results to DNS. The pattern motion in the nonlinear dynamics regime has been identified by DNS. We found that the transition between linear and nonlinear dynamics is determined at first order by the equilibrium between potential and kinetic energies.

The paper is organized as follows. We first describe the studied configuration in sect. 2. In sect. 3, we give a brief description of the computational methods. In sect. 4, we analyse and discuss the pattern motion regarding wavelength selection.

## 2 Problem description

In many practical situations, confinement and boundaries play a key role. This is particularly true for MHD flows (see for example [19]). Considering infinite conditions allows a generalization of the results. We consider an infinite fluid layer of a conducting fluid, confined between two rigid, horizontal plates, as sketched in fig. 1. The fluid is subject to the action of a steady, vertical magnetic field, and to the action of gravity. The temperatures are imposed at the walls, $T_b{}^\star$ at the bottom and $T_t{}^\star$ at the top, so that $\Delta T^\star = T_b{}^\star - T_t{}^\star > 0$. If this temperature difference exceeds a critical value, buoyancy force will become larger and the cavity will exhibit convection.

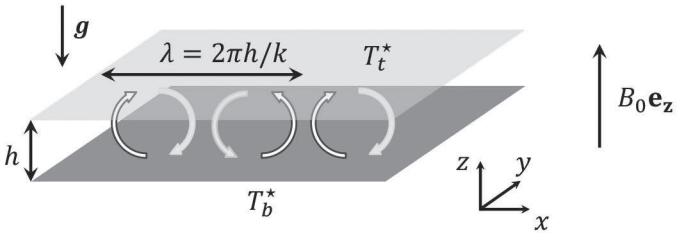


**Fig. 1.** Sketch of the configuration. The infinite horizontal walls are assumed to have an infinite thermal conductivity. The fluid is subjected to the action of gravity (buoyancy force) and of the Lorentz force.

Under the Oberbeck-Boussinesq approximation, the non-dimensional equations for the magnetoconvection are

$$\frac{\partial \mathbf{u}}{\partial t} + (\mathbf{u}\cdot\nabla)\mathbf{u} = -\nabla p + \triangle \mathbf{u} - \frac{Ra}{Pr} T \mathbf{e}_z + Ha^2 \mathbf{j}\times\mathbf{B}, \quad (1)$$

$$\frac{\partial T}{\partial t} + (\mathbf{u}\cdot\nabla)T = \frac{1}{Pr}\triangle T + \Gamma j^2, \quad (2)$$

$$\frac{\partial \mathbf{B}}{\partial t} = \frac{1}{Pm}\triangle \mathbf{B} + \nabla\times(\mathbf{u}\times\mathbf{B}). \quad (3)$$

We define the nabla operator in Cartesian coordinates $\nabla \equiv (\partial_x, \partial_y, \partial_z)$ and the Laplace operator $\triangle \equiv \nabla^2$. Equations (1), (2), and (3), respectively, are the Navier-Stokes equation, the heat transport equation (assuming incompressibility), and the induction equation, deduced from the Maxwell equations and generalized Ohm's law. In this paper, all $^\star$ quantities are dimensional parameters. Hence, the variables $\mathbf{u}$, $p$, $T$ and $\mathbf{B}$ represent the non-dimensional velocity, pressure, temperature and magnetic field, and $\mathbf{j}$ is the current density. The current density $\mathbf{j}$ can either be computed using Ohm's law or with Ampère's law. Additionaly, conservation of mass, electric charge and Maxwell-Thomson law read

$$\nabla\cdot\mathbf{u} = \nabla\cdot\mathbf{j} = \nabla\cdot\mathbf{B} = 0. \quad (4)$$

To non-dimensionalize the equations, we used the following characteristic parameters $t_0 = h^2/\nu$, $\mathcal{U} = \nu/h$, $B_0$ and $h$[1]. The non-dimensional temperature is defined by $T = (T^\star - T_t{}^\star)/\Delta T^\star$. The current density scale is $j_0 = \sigma\mathcal{U}B_0$. The fluid is confined between two plates located at $z = 0$ and $z = 1$. The additional non-dimensional parameter $\Gamma = j_0^2/\sigma\Delta T^\star\rho c_p$, with $c_p$ the specific heat is characteristic of the Joule dissipation into thermal energy. It is generally negligible in steady fields and it is not computed in the DNS nor in the LSA. Since $Pr$ and $Pm$ are only depending on physical properties of the fluid, they will be taken to be constant through the whole study. We used $Pr = 0.025$ and $Pm = 1.55 \cdot 10^{-6}$, as were used for liquid gallium [20]. $\Gamma \approx 10^{-13}$ can be neglected. In the configuration that was used for the DNS, we had $t_0 \simeq 1250\,\mathrm{s}$, with $h = 2\,\mathrm{cm}$.

As stated by Chandrasekhar [1], a vertical magnetic field modifies the critical value of the Rayleigh number

[1] With $\mathcal{U} = \nu/h$, $Rm \equiv Pm$. We have checked that $Rm$ based on the actual velocity is also much smaller than one.

**Table 1.** Values of the parameters charateristics of the DNS and LSA for the ten studied cases. The critical Rayleigh $Ra_c$ and wave number $k_c$ are obtained from the marginal stability analysis; the growth rate $s$ and the most unstable wave number $k_{\max}$ are obtained by LSA; the final wave number $k_\infty$ characterizes the pattern structure, and is obtained by DNS in the steady state regime.

| $\epsilon$ | 0.36 | 1.38 | 1.98 | 4.85 | 5.81 | 6.13 | 13.88 | 19.12 | 28.27 | 86.82 |
|---|---|---|---|---|---|---|---|---|---|---|
| $Ha$ | 18 | 36 | 9 | 0 | 18 | 36 | 9 | 18 | 0 | 0 |
| $Ra$ | $1 \cdot 10^4$ | $5 \cdot 10^4$ | $1 \cdot 10^4$ | $1 \cdot 10^4$ | $5 \cdot 10^4$ | $1.5 \cdot 10^5$ | $5 \cdot 10^4$ | $1.5 \cdot 10^5$ | $5 \cdot 10^4$ | $1.5 \cdot 10^5$ |
| $Ra_c$ | 7455 | $2.1 \cdot 10^4$ | 3391 | 1708 | 7455 | $2.1 \cdot 10^4$ | 3391 | 7455 | 1708 | 1708 |
| $s$ | 47.3 | 366 | 125 | 155 | 572 | 1220 | 633 | 1370 | 656 | 1440 |
| $k_{\max}$ | 4.55 | 5.23 | 3.78 | 3.50 | 4.42 | 5.32 | 4.28 | 4.91 | 4.08 | 4.67 |
| $k_c$ | 4.80 | 6.08 | 3.90 | 3.11 | 4.80 | 6.08 | 3.90 | 4.80 | 3.11 | 3.11 |
| $k_\infty$ | $\simeq 3.8$ | $\simeq 3.8$ | $\simeq 4.0$ | $\simeq 3.5$ | $\simeq 2$ | $\simeq 2.5$ | $\simeq 2.4$ | $\simeq 3.7$ | $\simeq 2.0$ | $\simeq 2.7$ |

$Ra_c$ beyond which convection appears. This threshold value scales as $Ra_c \sim \pi^2 Ha^2$ in the limit of high $Ha$ numbers. Recall that the parameter $\epsilon = (Ra - Ra_c)/Ra_c$ accounts for the distance to this threshold. We have interest in understanding the relative effects of the characteristic times $\tau_{\text{buo}}$ and $\tau_{\text{mag}}$. Therefore, we focus on the region of the parameter plane $(Ha, Ra)$ where those times remain of relatively close importance. We restrain ourselves to the region where $0 < Ha < 100$ and $0 < \epsilon < 20$. The computed points by DNS are given in table 1 and represented in fig. 2. The blue lines represent iso-lines of $\tau_\nu/\tau_{\text{buo}}$ and the orange lines represent the iso-lines of $\tau_{\text{mag}}/\tau_{\text{buo}}$. These lines can equivalently be understood as iso-lines of $Ra$ and $Ra/Ha^2$. One can note that the 2 points $\epsilon = 0.36$ and $\epsilon = 1.38$, the 3 points $\epsilon = 1.98$, $\epsilon = 5.81$ and $\epsilon = 6.13$, and the 2 points $\epsilon = 13.88$ and $\epsilon = 19.12$, approximately have the same ratio $\tau_{\text{mag}}/\tau_{\text{buo}}$= 35, 130 and 500, respectively. The analysis of the results for these 7 points will allow to understand the effect of $Ra/Ha^2$, of $Ha$ at the same $Ra$, and finally of $Ra$ at the same $Ha$.

## 3 Numerical methods

Two complementary methods are used to solve the case. We performed 3D DNS of the Rayleigh-Bénard instability with a vertical constant magnetic field and the corresponding Linear Stability Analysis (LSA). We first introduce the DNS code Jadim, that allows complete numerical resolution of the flow. We then present the LSA, which will give us the most unstable wave number $k_{\max}$ and the corresponding eigenfrequency $s$. The linear stability should accurately account for the transient growth of the stability.

### 3.1 Direct numerical simulations with Jadim

We solve this case using the finite volume code Jadim, in a bi-periodic square box in $x$ and $y$ directions of side 10. The mesh is chosen in order to respect the DNS criteria of Grötzbach [21]. The grid is composed of $N_x \times N_y \times N_z = 256 \times 256 \times 64$ points. The finite volume code Jadim has been already used in several different configurations. It uses a third order Runge-Kutta scheme for temporal integration. The spatial derivatives are calculated with second order accuracy. Incompressibility is achieved through a projection method. The viscous terms are calculated using a semi-implicit Crank-Nicolson scheme. The description of the numerical methods used in the computations can be found in Magnaudet *et al.* [22].

As long as the hypothesis of small magnetic Reynolds number is assumed, the magnetic field perturbation is $O(Rm)$ compared to the other fields, and induction can be neglected. In this case, Faraday's law reduces to $\nabla \times \mathbf{E} = 0$, with $\mathbf{E}$ the electric field, and it allows to write the electric field as the gradient of a potential $\Phi$. This is the so-called quasi-static approximation. Therefore, Ohm's law reduces to:

$$\mathbf{j} = -\nabla\Phi + \mathbf{u} \times \mathbf{e}_z. \tag{5}$$

Electric charge conservation $\nabla \cdot \mathbf{j} = 0$ is ensured by a Poisson equation on the electric potential $\Phi$:

$$\triangle\Phi = \nabla \cdot (\mathbf{u} \times \mathbf{e}_z). \tag{6}$$

This method is used in the DNS to compute the Lorentz force. Equation (6) is solved using the PETSc library [23]. A first order scheme was used to compute the gradient of $\Phi$. As boundary conditions for the velocity, we consider a no-slip condition. We assume infinite thermal conductivity of the walls. This translates into a Dirichlet's condition for the temperature at the walls. In the same way we assume walls as perfect electrical conductors. In terms of electric potential, this amounts to saying that the electric potential $\Phi$ is imposed at the walls. Without loss of generality, we can assume that $\Phi = 0$. Physically, this corresponds to enclosing the liquid between highly thermally and electrically conducting, and non-magnetic plates (such as copper, see for example [16]). As Joule dissipation is not significant for steady fields and relatively low $Ha$ numbers, this source term is not computed in the DNS. For $t < 0$, the fluid is at rest at uniform temperature; at $t > 0$ the temperature of the bottom is set to 1. The non-dimensional fluid velocity field is initiated with random values of magnitude $10^{-15}$. We compared the numerical results obtained for $64 \times 256 \times 256$ and $128 \times 512 \times 512$ mesh grids at $Ha = 36$, $Ra = 1.5 \cdot 10^5$ to verify the numerical convergence. This case has been chosen because it corresponds to the thinnest Hartmann layer in our study. From this comparison we estimate that the velocity profile is calculated with an error of 4%.

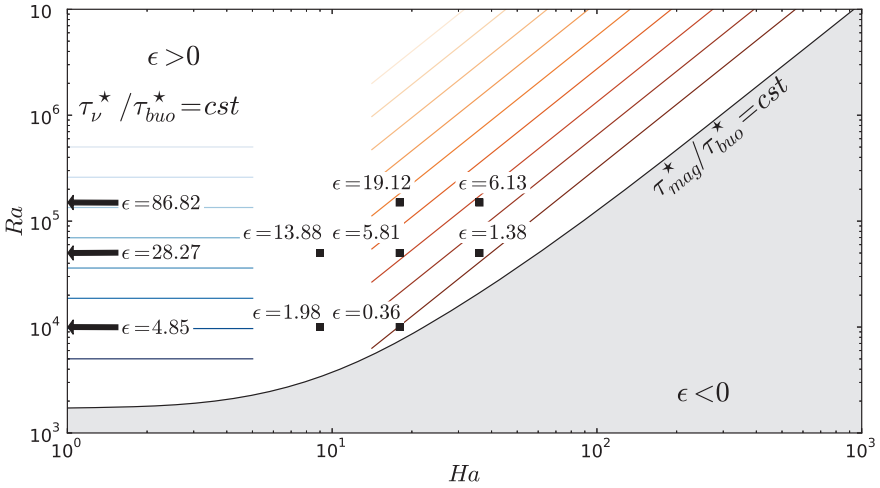


**Fig. 2.** DNS points displayed in the parameter space $(Ha, Ra)$. The arrows show the three cases at $Ha = 0$. The marginal stability curve is defined by $\epsilon = 0$. All points located above this curve ($\epsilon > 0$, white region) are unstable and will exhibit convection. Iso-lines of $\tau_{\rm vis}/\tau_{\rm buo}$ are drawn in blue by and iso-lines of $\tau_{\rm mag}/\tau_{\rm buo}$ are drawn in orange.

### 3.2 Linear stability analysis

We follow here Chandrasekhar in establishing the algebraic linear system for the amplitudes of the perturbed fields. The equilibrium solution of the system (3) is given by $(\mathbf{u}, T, \mathbf{B}) = (\mathbf{0}, 1-z, 1\mathbf{e}_z)$, and this solution is used as the base state at $t = 0$. We linearly perturb this base state. We call the vertical velocity perturbation $w$, the temperature perturbation $\vartheta$, and the vertical magnetic field perturbation $b_z$. Here, the current density is given by Maxwell-Ampère's law, $\mathbf{j} = \frac{1}{Pm}\nabla\times\mathbf{b}$. Taking $-\nabla\times\nabla\times(1)$ ensures the elimination of the gradient terms and of the complex terms. We then linearize (2) and the components along the $z$-axis of $-\nabla\times\nabla\times(1)$ and (3). Finally we have the set of equations (7) to (9)

$$\frac{\partial\triangle w}{\partial t} = \triangle^2 w + \frac{Ra}{Pr}\left(\frac{\partial^2\vartheta}{\partial x^2}+\frac{\partial^2\vartheta}{\partial y^2}\right) + \frac{Ha^2}{Pm}\frac{\partial\triangle b_z}{\partial z}, \quad (7)$$

$$\frac{\partial\vartheta}{\partial t} = \frac{1}{Pr}\triangle\vartheta + w, \quad (8)$$

$$\frac{\partial b_z}{\partial t} = \frac{1}{Pm}\triangle b_z + \frac{\partial w}{\partial z}. \quad (9)$$

Note that the Joule dissipation term does not appear any more, since it is a second order term. However, this approach, compared to DNS, takes into account the time-dependent perturbation of the magnetic field. The LSA results have confirmed that it is negigible. Considering disturbances as two-dimensional waves in the horizontal plane of assigned wave numbers $k_x$ and $k_y$ in $x$- and $y$-directions gives

$$\begin{pmatrix} w \\ \vartheta \\ b_z \end{pmatrix} = \underbrace{\begin{pmatrix} W(z) \\ \Theta(z) \\ \mathcal{B}(z) \end{pmatrix}}_{\mathbf{X}(z)} \exp(i(k_x x + k_y y) + st). \quad (10)$$

Here, $W(z)$, $\Theta(z)$ and $\mathcal{B}(z)$ are the initial amplitudes of the disturbances, and $s$ is growth rate of the disturbance.

Using the form given by eq. (10) in system (7), it is possible to write the equations in the form of an eigenvalue problem

$$s\mathcal{L}_1\mathbf{X}(z) = \mathcal{L}_2\mathbf{X}(z), \quad (11)$$

where:

$$\mathcal{L}_1 = \begin{pmatrix} (D^2-k^2) & 0 & 0 \\ 0 & 1 & 0 \\ 0 & 0 & 1 \end{pmatrix}, \quad (12)$$

$$\mathcal{L}_2 = \begin{pmatrix} (D^2-k^2)^2 & -\frac{Ra}{Pr}k^2 & \frac{Ha^2}{Pm}[D(D^2-k^2)] \\ 1 & \frac{1}{Pr}(D^2-k^2) & 0 \\ D & 0 & \frac{1}{Pm}(D^2-k^2) \end{pmatrix}, \quad (13)$$

with $D \equiv \frac{\mathrm{d}}{\mathrm{d}z}$ and $k^2 = k_x^2 + k_y^2$. Each block $\mathcal{L}_{2,mn}$ represents the action of the $n$-th variable on the $m$-th variable. This system is solved with finite differences using second order schemes. The details of calculation are given in appendix A. Following the same boundary conditions as for the DNS, we consider infinitely thermally and electrically conducting walls. If the external media is a perfect electrical conductor, the time-dependant perturbation of the magnetic field inside it is instantly relaxed. Therefore we can assume a homogeneous Dirichlet's condition for the perturbation of the magnetic field. The same condition goes for the temperature perturbation. The boundary conditions, following the no-slip condition, the continuity equation, and the perfectly conducting walls, are then

$$W = DW = \Theta = \mathcal{B} = 0 \quad (14)$$

for $z = 0, 1$. Solving the system (11) gives the growth rate (or eigenfrequency) $s$ of the system and the most un-

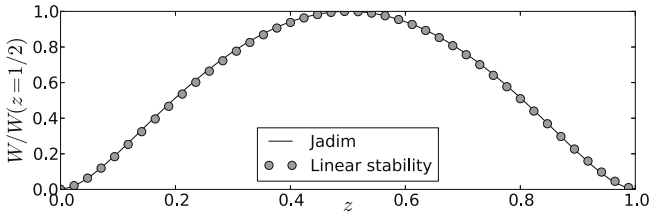


**Fig. 3.** Comparison of vertical velocity profiles obtained with DNS (solid line) and LSA (dots) in the linear regime. Both curves are normalized by their value at $z = 1/2$.

stable wave number $k_{\max}$, that corresponds to an eigenvector $\mathbf{X}(z) = (W(z), \Theta(z), \mathcal{B}(z))$. The case $s = 0$ was solved by Chandrasekhar [1] and gives the values of $Ra_c$ as a function of $Ha$. It corresponds to the solution of $\epsilon = 0$, represented by the boundary between the white and grey regions in fig. 2. We observe a very good agreement between the LSA results and Chandrasekhar's predictions. We have extended this analysis to overcritical values $Ra > Ra_c$, in order to assess the transient growth of the instability. We have checked that the difference in $s$ between grids of size 256 and 512 was less than 1%.

## 4 Results and discussion

### 4.1 Short and large timescales behavior

In the DNS, the system is initiated with a uniform cold temperature $T = 0$, and the fluid is at rest, with a small random noise. The temperature at the bottom wall is imposed at $T = 1$. The high thermal conductivity of the fluid (*i.e.* low $Pr$) allows the establishment of a linear conducting profile in a few time steps. From then, buoyant motion starts to rise in the quiescent liquid. During those first instants, a profile of vertical velocity matches the profile given by linear stability (*i.e.* eigenvector). This is found to be valid for any profile taken at any random coordinates $(x, y)$. Figure 3 shows one profile obtained with Jadim, compared with the linear stability, both normalized by their value at $z = 1/2$. The agreement between the two approaches is valid until the end of the linear regime. Here we define the linear regime by the validity of the LSA that corresponds to the instability growth.

Next, we consider the quantity

$$\overline{w^{\star 2}(z^\star = h/2)} = \frac{1}{S} \iint_S w^{\star 2}(z^\star = h/2) \mathrm{d}x^\star \mathrm{d}y^\star, \qquad (15)$$

with $w^\star$ the velocity in SI units and $S$ the surface of the wall. This quantity represents the contribution of the vertical component of velocity to kinetic energy, averaged in the mid-plane. The evolution of this quantity is shown in fig. 4 for both DNS and LSA. Here, $w^\star$ is scaled by the characteristic buoyant velocity. We observe a phase where the velocity grows as $\exp(st)$, where $s$ is the LSA growth rate of the instability. Its value depends both on $Ra$ and $Ha$, which will be later discussed. All the curves collapse

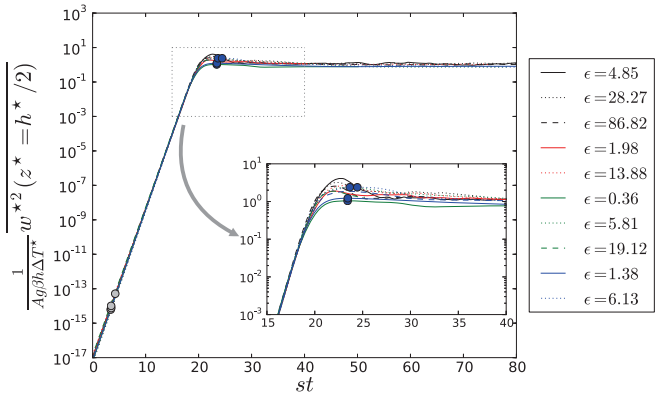


**Fig. 4.** Dynamic behavior by DNS and LSA for all the computed points. We used the average value of the factor $A$ to normalize the curves. Inset: zoom on the transition between the linear and nonlinear regime.

into one master curve during the exponential growth of the instability, when plotted as a function of $st$. After this exponential growth, nonlinear effects become significant and the flow is reorganized until the stationary stage is reached.

The simulations show that for $\epsilon = 1.38$ and $\epsilon = 5.81$ which correspond to the same $Ra$ and different $Ha$, the final values of $\overline{w^2(z = 1/2)}$ are identical. Moreover, the plateau value in the nonlinear regime is a function of $Ra$. Based on this results, it is possible to estimate the final value of $\overline{w^{\star 2}(z^\star = h/2)}$ by a simple energy balance between kinetic energy and potential energy. This condition reads

$$\overline{w^{\star 2}(z^\star = h/2)} = A\, g\beta h \Delta T^\star, \qquad (16)$$

where $A$ is a factor to be determined. This relation is equivalent to $W^2 \sim Ra$. We stress that this estimate does not take into account the Lorentz and viscous forces. Consequently, the DNS results show that all the curves can be superimposed in the linear and nonlinear regimes, as seen in fig. 4. The value of $A$ using the DNS results is found to be $A = 0.10 \pm 0.02$ for all the simulations.

Around the transition between the linear and nonlinear regimes ($st \approx 20$ for our initial conditions), we do not observe an exact overlap. The simulations display that $Ha$ contributes significantly to the amplitude of the yield kinetic energy. In conclusion, the linear regime is governed by $(Ra, Ha)$, and the nonlinear regime by $Ra$.

In fig. 4, the timescale was obtained from $s$ given by LSA (eq. (11) and table 1). Based on LSA, a systematic computation of $s$ has been realised for $10^3 \leq Ra \leq 1.5{\cdot}10^5$ and $0 \leq Ha \leq 100$ (fig. 5). We observe that $s$ is a decreasing function of $Ha$ at constant $Ra$ (damping effect of magnetic field), and an increasing function of $Ra$ at constant $Ha$. Moreover $\epsilon$ is not a self-similarity parameter and $s$ is not an univoque function of $\epsilon$. For any value of $(Ha, Ra)$ in the variation range studied by LSA, it is now possible to determine the $s$ value from fig. 5 which fixes the scaling in the linear regime. Our computed points in DNS appear in red circles in this figure.

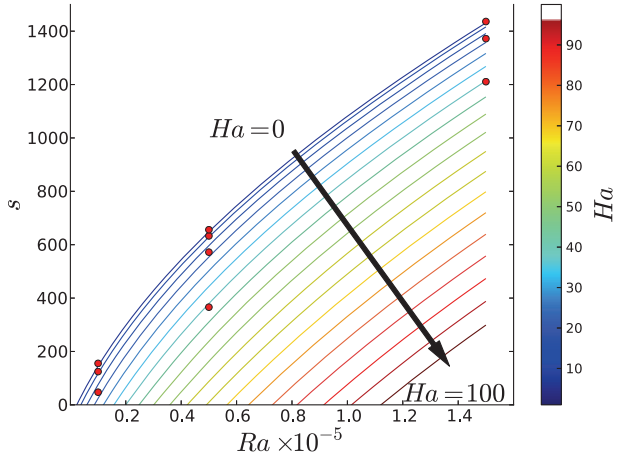


**Fig. 5.** Growth rate $s$ *vs.* $Ra$ for $0 \leq Ha \leq 100$. The step of 5 in $Ha$ is fixed for two adjacent isolines. The points computed with DNS are represented by the red circles.

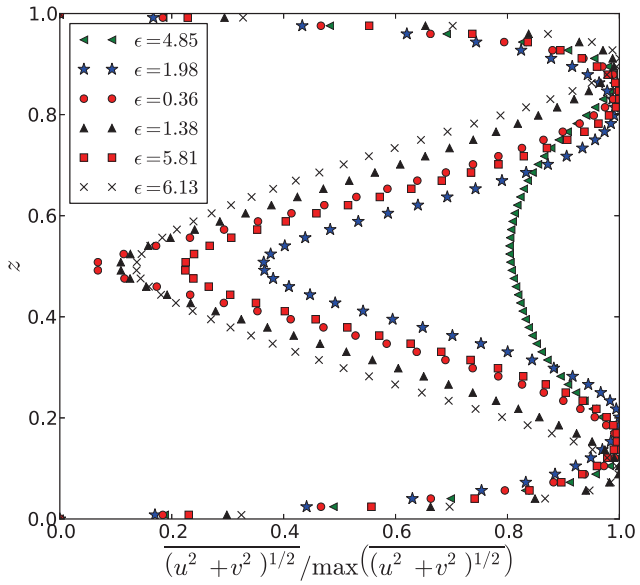


**Fig. 6.** Time and space averaged profiles of tangential velocity in the steady state nonlinear regime, for the DNS referenced in table 1. The curves are normalized to their maximum value and the bar denotes averaging in $(x, y)$-directions.

In fig. 6, we show profiles of time and space averaged velocity tangential to the Hartmann walls (orthogonal to the magnetic field) for several points. Without magnetic field ($Ha = 0$, $Ra = 10^4$ and $\epsilon = 4.85$), the boundary layer thickness is of order $\delta \simeq 0.14$ (defined as the distance to the wall corresponding to the maximum of the tangential velocity). When a magnetic field is applied, Hartmann layers are likely to form and modify the velocity field. In the case $Ha = 9$ and $Ra = 10^4$ ($\epsilon = 1.98$), the turbulent motion is suppressed compared to the case where $Ha = 0$ and the boundary layer is thicker, $\delta \simeq 0.19$. Further increase of $Ha$ shows a thinning of the boundary layer thickness due to the magnetic field effects. Thus, from $Ha = 9$, we find that $\delta$ decreases with $Ha$ accordingly to a general trend in the Hartmann problem, coupled with thermal effects. It is also noticeable that the points $\epsilon = 0.36$ and $\epsilon = 5.81$ at the same $Ha = 18$ have a same boundary layer thickness: $\delta \simeq 0.14 \pm 0.01$. A same boundary layer thickness is also measured for the points $\epsilon = 1.38$ and $\epsilon = 6.13$ ($Ha = 36$): $\delta \simeq 0.09 \pm 0.01$.

### 4.2 Patterns motion

In this section we discuss four characteristic cases which are physically representative ($\epsilon = 0.36$, 1.38, 5.81 and 6.13). DNS allows to determine the motion structures and their evolutions in time for the four values of $\epsilon$. The spatial distribution of vertical velocity at $z = 1/2$ was analyzed by Fourier transform and the velocity structures were characterized by their wave vectors. In Supplementary Material, motion pictures of the patterns are presented in regard of the time evolutions of the kinetic energy, its spectral density, and the 2D wave vector distribution in the plane orthogonal to the magnetic field and the gravity (see videos). The movies show that the structures in linear and nonlinear regimes ($st < 20$ and $st > 20$, respectively) are strongly different. Figure 7, extracted from movies, presents three snapshots of $W$ in the mid-plane, normalized by the instantaneous amplitude for the four $\epsilon$ value.

Each row corresponds to one DNS and each column to a snapshot in the linear regime, at the peak value of the kinetic energy in the mid-plane, and in the nonlinear steady state. They respectively correspond to the blue, grey and white circles in fig. 4.

In the linear part of the fig. 4, the structures develop into periodic and isotropic cells independent of time (first column of fig. 7). The spectral analysis of the patterns shows that the wave number $k_{\max}$ in DNS is very well predicted by LSA in the early phase. For the four simulated cases, $k_{\max}$ is lower but close to critical wave number at the marginal stability $k_c$. These results can be seen in fig. 8 which shows, as an example, the energy spectral density at different times for $\epsilon = 0.36$. The peak at $t = 0.06$ perfectly matches the $k_{\max}$ prediction of LSA. This result is valid for all the computed points in table 1. The LSA at supercritical values of $\epsilon$ improves the prediction of the linear behavior compared to the classic marginal theory [1].

In fig. 8 we found that $k_{\max} < k_c$ in the linear phase. However this result cannot be generalized for a large range of $(Ha, Ra)$. Figure 9 compares the variations of $k_{\max}$ and $k_c$ for $0 \leq Ha \leq 40$ and $10^4 \leq Ra \leq 1.5\ 10^5$, obtained by LSA. First we note that $k_c$ increases drastically with $Ha$. Secondly, for $Ha \lesssim 10$, $k_{\max}$ increases with $Ra$. However, for higher $Ha$ values, $k_{\max}$ decreases, then increases again with $Ra$. This means that $k_{\max}$ can be smaller or larger than $k_c$, depending on $Ha$ and $Ra$. Thirdly, for all values $Ha$, $k_{\max}$ seems to reach a plateau value when $Ra$ increases. This plateau value is larger than $k_c$ at low $Ha$ and smaller than $k_c$ at high $Ha$. This asymptotic value is weakly dependent on $Ha$. Hence the effect of the magnetic field does not seem to play a significant role at values of $Ra$ much larger than $Ra_c$. On the other hand, close to $Ra_c$, as for the marginal stability curve, $Ha$ has a strong influence on the velocity structures.

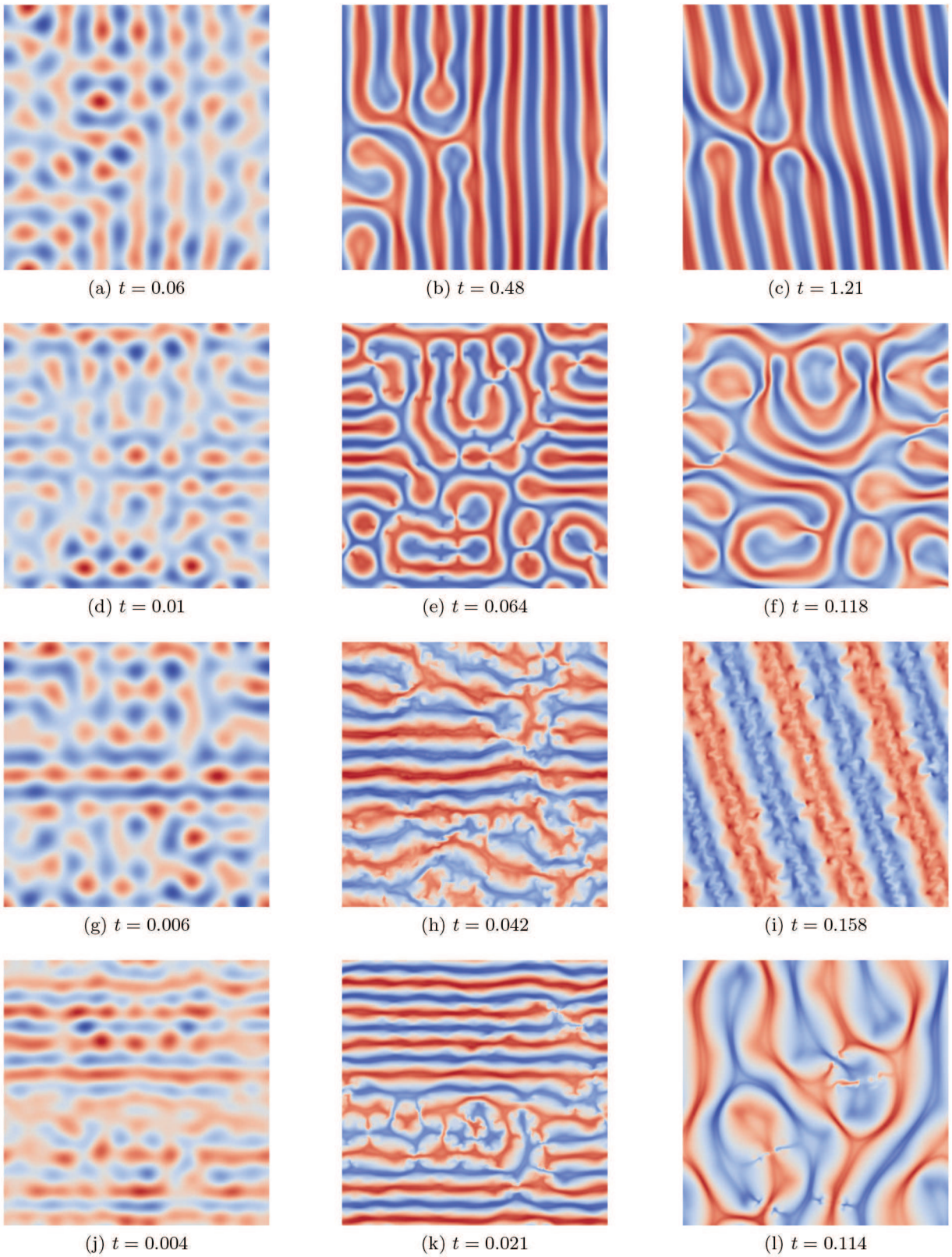


**Fig. 7.** Snaphots of normalized vertical velocity for different times at $z = 1/2$ for $\epsilon = 0.36$ (panels (a) to (c)), $\epsilon = 1.38$ (panels (d) to (f)), $\epsilon = 5.81$ (panels (g) to (i)), and $\epsilon = 6.13$ (panels (j) to (l)), by DNS (red is positive and blue is negative). The first column corresponds to a snapshot during the linear regime, the second one is taken during the transition between the linear and nonlinear regime (the times are indicated in fig. 4), and the third one is characteristic of the steady state nonlinear regime. The snapshots are extracted from the DNS movies.

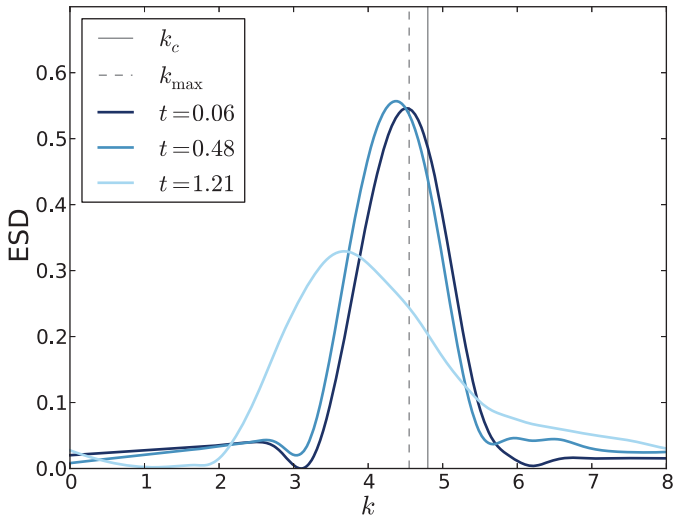


**Fig. 8.** Energy spectral density for $\epsilon = 0.36$ in the linear regime ($t = 0.06$), at the maximum of the kinetic energy ($t = 0.48$) and in the steady state nonlinear regime ($t = 1.21$). The wave number values at the marginal stability $k_c$ and calculated by the LSA $k_{\max}$ are given for comparison.

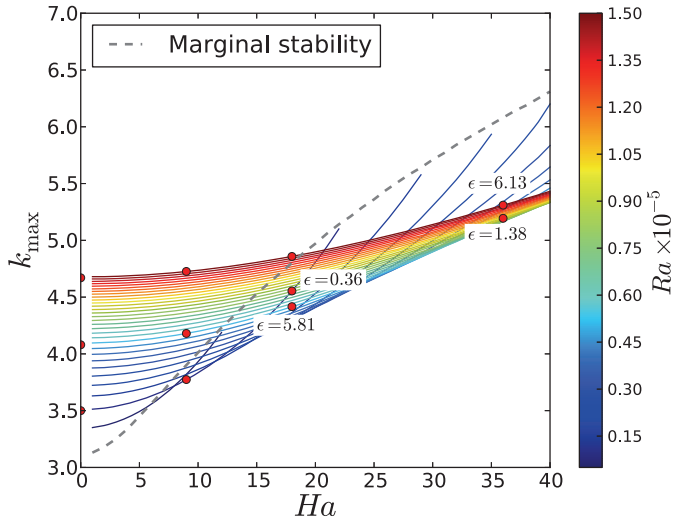


**Fig. 9.** Wave number $k_{\max}$ *vs.* $Ha$. Each colored curve corresponds to a constant $Ra$.

This can be explained by considering that the characteristic width of the rolls is determined by the product of the characteristic time of cooling and the velocity close to the upper wall. This velocity decreases with $Ha$ due to the Lorentz force.

After linear growth, a transition phase takes place, where nonlinear effects come into play, before reaching the stationary state. The structures evolve continuously and we found that this evolution is not characterized by a first order transition. For the four $\epsilon$ values, the wave number characteristic of the velocity structure is closed to $k_{\max}$ at the maximum kinetic energy (fig. 8). At this peak, nonlinear effects become dominant and the wave number decreases towards a steady value that we name $k_\infty$.

The steady state velocity patterns in nonlinear regime are presented in the right column of fig. 7, and all the structures are characterized by their 2D wave vector distribution in fig. 10. The blue circle corresponds to $k_c$ predicted by Chandrasekhar [1] and the red dashed circle is $k_{\max}$ predicted by LSA. During the linear phase, the energy is concentrated on the circle of radius $k_{\max}$ (see videos in Supplementary Material and the curve for $t = 0.06$ in fig. 8). In the case $\epsilon = 0.36$ the small cells of the linear regime merge into slightly larger rolls (fig. 7(b)) which persist in time. In the steady state the velocity structure is frozen-like. In fig. 10(a), we see that most of the energy is localized in one direction associated to a lamellar structure. The wave number decreases down to an asymptotic value $k_\infty \simeq 3.7$, which remains close to $k_{\max} = 4.55$.

In the case $\epsilon = 1.38$, the cells merge and form larger roll-like structures. These tortuous structures remain stable and evolve very slowly. The norm of the wave vector is lower than $k_{\max}$, around a value $k_\infty \simeq 4.0$. The main difference in comparison with the case $\epsilon = 0.36$ is that the energy tends to be istropically distributed. These tortuous structures seem to be related to spiral defect chaos (SDC) observed by Morris *et al.* [24].

In case $\epsilon = 5.81$, at the peak of transition (fig. 7(h)), the cells tend to reorganize in tortuous rolls, but this structure is only transient. It then degenerates in large cells around $k \simeq 2.5$ before further reorganizing in parallel rolls in the stationary regime with a wave number $k_\infty \simeq 2.0$ (fig. 7(i)). These rolls display an oscillation which seems to be linked to a secondary instability [11]. In this case, the energy in Fourier space is mainly localised in a unique direction as seen in fig. 10(c). The secondary peak at $k = 6.0$ is characteristic of the smaller structures of the rolls. In this case the dominant wave number in the stationary regime departs significantly from LSA.

The behavior of the flow for $\epsilon = 6.13$ during the transition is similar to the one for $\epsilon = 5.81$. At the beginning of the transition, the cells merge in rolls (as seen in the DNS movies). Subsequently, these rolls transform in cell patterns, which persist contrary to the previous case. This steady state is similar to the case $\epsilon = 1.38$ but with a different final wave number $k_\infty \simeq 2.5$. The energy density spreads towards smaller wavelength (see Supplementary videos).

The analysis of these four typical cases ($\epsilon = 0.36$, 1.38, 5.81 and 6.13) shows that the results seem to be coherent. The two cases $\epsilon = 0.36$ and $\epsilon = 1.38$ correspond to the same $Ra/Ha^2 \approx 35$. On the other hand, $\epsilon = 5.81$ and $\epsilon = 6.13$ correspond to $Ra/Ha^2 \approx 130$. For isolines of $Ra/Ha^2$ close to the marginal stability curve, the patterns in the steady state nonlinear regime are characterized by a wave number lower but close to $k_{\max}$ (obtained from LSA). For larger values of $Ra/Ha^2$, the characteristic sizes of the structures are larger and $k_\infty$ is smaller than $k_{\max}$. In this case the transition dynamics leading to the steady state nonlinear regime is more complex and shows permanent reorganization due to higher $Ra$.

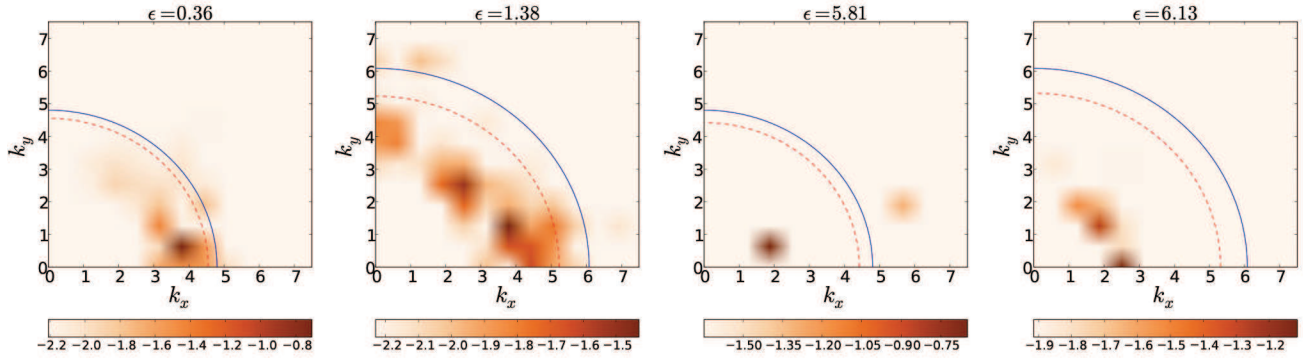


(a) $t = 1.21$ (b) $t = 0.118$ (c) $t = 0.158$ (d) $t = 0.114$

**Fig. 10.** 2D normalized energy spectra of the vertical velocity $W(z = 1/2)$, for $\epsilon = 0.36$ $\epsilon = 1.38$, $\epsilon = 5.81$, and $\epsilon = 6.13$ in the steady state nonlinear regime. The data are normalized by the total energy. The colors are in log-scale. These spectra correspond to the snapshots of the third column in fig. 7. The marginal wave number $k_c$ (solid blue circle) and $k_{\max}$ (dashed red circle) calculated by LSA are given for comparison.

Considering all the studied cases, the DNS seems to display a structural transition between lamellar and tortuous when $Ha$ increases and $\epsilon < 10$. Indeed, at $Ha = 9$ and 18 ($\epsilon = 1.98$, $\epsilon = 0.36$ and $\epsilon = 5.81$), the patterns are lamellar; at $Ha = 36$ ($\epsilon = 1.38$ and $\epsilon = 6.13$), the patterns are tortuous lamellar. This tortuous structure could be understood as a coupling effect of buoyancy force and Lorentz force acting of the velocity field in the three directions. The joint effect of these two forces is to create a torque which bends the lamellar structures if $Ha$ is high enough. For $\epsilon > 10$ ($\epsilon = 13.88$ and $\epsilon = 19.12$), the structures become similar to thermoconvection without magnetic effect. These two cases are far enough from the marginal stability curve and the buoyancy force becomes dominant.

## 5 Concluding remarks

In this paper, we studied the transient dynamics of a liquid metal in magnetoconvection. We computed the velocity patterns by DNS for various value of $\epsilon = (Ra - Ra_c)/Ra_c$ corresponding to intermediate $(Ha, Ra)$ values. The characteristic lengths of the patterns were measured during the transient dynamics: linear regime, nonlinear transition and steady regime. We have developed a LSA code, in order to determine the growth rate and the wave number of the instability. We observe a very good agreement between the DNS results in the linear regime and the LSA predictions. From the DNS, the wave vectors characteristic of the structures appear to be isotropic and the maximum of the energy density matches the value $k_{\max}$ of the LSA. It is to note that the methods for computing the Lorentz force differ in the two approaches. In the DNS we used the quasi-static model and in the LSA we solved for the perturbation of $\mathbf{B}$. Both methods should agree in the $Pm = 0$ limit. Here these approaches are consistent, owing to the smallness of $Pm$. We found that the dynamics is self-similar except around the transition between the two regimes where the total energy of the system yields a maximum. The time scaling in the linear regime is based on the growth rate, and in the steady state nonlinear regime, the energy scaling is given by $Ra$ and is independent of $Ha$ at first order.

In the steady state nonlinear regime the patterns present large differences with $Ra$ and $Ha$. For cases neighbouring the marginal stability ($\epsilon = 0$) and with a same $Ra/Ha^2$ ratio, the wave number $k_\infty$ is lower, but very close to $k_{\max}$. For cases far away from the marginal stability and at constant $Ra/Ha^2$, the wave number $k_\infty < k_{\max}$. Therefore, an increase in $Ra/Ha^2$ generates a decrease in $k_\infty$. Furthermore, the structure types are determined by $Ha$ in the steady state nonlinear regime. For $Ha = 9$ and 18, we observe a lamellar structure. Increasing to $Ha = 36$ shows that there is a structural transition: the rolls become tortuous. This study will be extended to a large range of $\epsilon$ values and to frequency effects when AC magnetic fields are applied.

The authors greatly acknowledge the help of Annaïg Pedrono for the numerical developments in the Jadim code. This work was granted access to the HPC resources of CALMIP supercomputing center. Financial support from the french Nuclear Energy Center (CEA) in Cadarache and from the ECM company in Grenoble are acknowledged.

## Appendix A. Finite differences schemes for stability analysis

We give in this appendix the numerical schemes that were used for the linear stability analysis. The operators in equations (12) and (13) can be expressed with finite differences, in order to solve the linear system (11).

## Appendix A.1. Numerical schemes

Let us consider the vector $x$ that either stands for $W$, $\Theta$, or $\mathcal{B}$ and we discretize in the $z$-direction and for a number of points $N_z$, the space step is $\Delta z = \frac{1}{N_z}$. We choose the following second order schemes to approximate the derivatives:

$$x_i' = \frac{x_{i+1} - x_{i-1}}{2\Delta z}, \tag{A.1}$$

$$x_i'' = \frac{x_{i+1} + x_{i-1} - 2x_i}{\Delta z^2}, \tag{A.2}$$

$$x_i''' = \frac{x_{i+2} - x_{i-2} - 2x_{i+1} + 2x_{i-1}}{2\Delta z^3}, \tag{A.3}$$

$$x_i^{(4)} = \frac{x_{i+2} + x_{i-2} - 4x_{i+1} - 4x_{i-1} + 6x_i}{\Delta z^4}. \tag{A.4}$$

Let us express $\mathbf{X}$ and the operators $\mathcal{L}_1$ and $\mathcal{L}_2$ from eq. (11) with finite differences

$$\mathbf{X} = (W_1, \cdots, W_{N_z}, \Theta_1, \cdots, \Theta_{N_z}, \mathcal{B}_1, \cdots, \mathcal{B}_{N_z})^T, \tag{A.5}$$

$$\mathcal{L}_k = \begin{pmatrix} \mathcal{L}_{k,11} & \mathcal{L}_{k,12} & \mathcal{L}_{k,13} \\ \mathcal{L}_{k,21} & \mathcal{L}_{k,22} & \mathcal{L}_{k,23} \\ \mathcal{L}_{k,31} & \mathcal{L}_{k,32} & \mathcal{L}_{k,33} \end{pmatrix}, \tag{A.6}$$

with $k = 1$ or 2. Each matrix $\mathcal{L}_{k,ij}$ is a $N_z \times N_z$ matrix. As shown in the following paragraph, the matrices $\mathcal{L}_1$ and $\mathcal{L}_2$ depend on $Ra$, $Ha$, $Pr$, $Pm$ and $k$.

## Appendix A.2. Expression of the matrices

We can note that the matrices $\mathcal{L}_{1,ij}$ and $\mathcal{L}_{2,ij}$ will be $(n+1)$-diagonal where $n$ is the order of derivation. Replacing the terms in eqs. (1), (2) and (3) with the expressions given by eqs. (A.1) to (A.4) reads

$$\mathcal{L}_{1,11} = \frac{1}{\Delta z^2} \begin{pmatrix} a_{11}^{11} & a_{11}^{12} & 0 & \cdots & 0 \\ 1 & -2 & 1 & \ddots & \vdots \\ 0 & \ddots & \ddots & \ddots & 0 \\ \vdots & \ddots & 1 & -2 & 1 \\ 0 & \cdots & 0 & a_{11}^{N_z,N_z-1} & a_{11}^{N_z,N_z} \end{pmatrix}, \tag{A.7}$$

$$\mathcal{L}_{1,22} = \mathbb{I}, \tag{A.8}$$

$$\mathcal{L}_{1,33} = \mathbb{I}, \tag{A.9}$$

$$\mathcal{L}_{1,ij,i\neq j} = 0, \tag{A.10}$$

where $\mathbb{I}$ is the identity matrix. The terms $a_{11}^{11}$, $a_{11}^{12}$, $a_{11}^{N_z,N_z-1}$ and $a_{11}^{N_z,N_z}$ will be given by the boundary conditions. Those matrices represent the terms on the left side of the equations, and except for $\mathcal{L}_{1,11}$, there is no derivative term which implies the matrices to be diagonal. The $\mathcal{L}_{2,ij}$ matrices represent the coupling between the different equations. Let $b_{ij}^{(0)}$, $b_{ij}^{(-1)}$, $b_{ij}^{(-2)}$, $b_{ij}^{(+1)}$, $b_{ij}^{(+2)}$ be the main, first lower, second lower, first upper and second upper diagonal terms of the matrix. The inner aspect of the matrix is

$$\mathcal{L}_{2,ij} = \begin{pmatrix} \ddots & \ddots & \ddots & \ddots & \ddots \\ & b_{ij}^{(-2)} & b_{ij}^{(-1)} & b_{ij}^{(0)} & b_{ij}^{(+1)} & b_{ij}^{(+2)} \\ & & \ddots & \ddots & \ddots & \ddots & \ddots \end{pmatrix}. \tag{A.11}$$

The other terms are all equal to zero. The two first and the two last lines will be given by the boundary conditions. We can first express the $\mathcal{L}_{2,11}$, $\mathcal{L}_{2,22}$, $\mathcal{L}_{2,33}$ matrices. The $\mathcal{L}_{2,11}$ matrix is pentadiagonal and we have

$$b_{11}^{(0)} = \frac{6}{\Delta z^4} + 4\frac{k^2}{\Delta z^2} + k^4, \tag{A.12}$$

$$b_{11}^{(+1)} = b_{11}^{(-1)} = -\frac{4}{\Delta z^4} - \frac{2k^2}{\Delta z^2}, \tag{A.13}$$

$$b_{11}^{(+2)} = b_{11}^{(-2)} = \frac{1}{\Delta z^4}. \tag{A.14}$$

The $\mathcal{L}_{2,22}$ et $\mathcal{L}_{2,33}$ matrices are tridiagonal, hence $b_{22}^{(+2)} = b_{22}^{(-2)} = b_{33}^{(+2)} = b_{33}^{(-2)} = 0$. We can express the other terms as

$$b_{22}^{(0)} = -\frac{1}{Pr}\frac{k^2+2}{\Delta z^2}, \tag{A.15}$$

$$b_{22}^{(+1)} = b_{22}^{(+1)} = \frac{1}{Pr}\frac{1}{\Delta z^2}, \tag{A.16}$$

$$b_{33}^{(0)} = -\frac{1}{Pm}\frac{k^2+2}{\Delta z^2}, \tag{A.17}$$

$$b_{33}^{(+1)} = b_{33}^{(+1)} = \frac{1}{Pm}\frac{1}{\Delta z^2}. \tag{A.18}$$

The $\mathcal{L}_{2,13}$ and $\mathcal{L}_{2,31}$ are also pentadiagonal and tridiagonal matrices and the diagonal terms can be expressed as

$$b_{13}^{(0)} = 0, \tag{A.19}$$

$$b_{13}^{(+1)} = -b_{13}^{(-1)} = \frac{Ha^2}{Pm}\left(\frac{1}{\Delta z^3} + \frac{k^2}{2\Delta z}\right), \tag{A.20}$$

$$b_{13}^{(+2)} = b_{13}^{(-2)} = \frac{1}{2\Delta z^3}, \tag{A.21}$$

$$b_{31}^{(0)} = 0, \tag{A.22}$$

$$b_{31}^{(+1)} = -b_{31}^{(-1)} = \frac{1}{2\Delta z}. \tag{A.23}$$

Since the magnetic field and the temperature do not influence each other, the $\mathcal{L}_{2,23}$ and $\mathcal{L}_{2,32}$ are empty. If we took in consideration the Joule dissipation, the $\mathcal{L}_{2,32}$ would not be zero, but since the equations were linearised and the Joule dissipation is a second order term, it does not appear here. $\mathcal{L}_{2,12}$ and $\mathcal{L}_{2,21}$ are diagonal matrices and are expressed as

$$\mathcal{L}_{2,12} = -\frac{Ra}{Pr}k^2\mathbb{I}, \qquad \mathcal{L}_{2,21} = \mathbb{I}. \tag{A.24}$$

## References


1. S. Chandrasekhar, *Hydrodynamic and Hydromagnetic Stability* (Clarendon Press, 1961).
2. R. Moreau, Prog. Crystal Growth **38**, 161 (1999).
3. H. Branover, *Metallurgical Technologies, Energy Conversion, and Magnetohydrodynamic Flows*, Vol. **148** (AIAA, 1993).
4. Ch. Journeau, P. Piluso, J.F. Haquet, S. Saretta, E. Boccaccio, J.M. Bonnet, *Proc. ICAPP* (2007).
5. E. Taberlet, Y. Fautrelle, J. Fluid Mech. **159**, 409 (1985).
6. J.M. Aurnou, P.L. Olson, J. Fluid Mech. **430**, 283 (2001).
7. U. Burr, U. Müller, Phys. Fluids **13**, 3247 (2001).
8. N.O. Weiss, M.R.E. Proctor, *Magnetoconvection* (Cambridge University Press, 2014).
9. Y. Nakagawa, Nature **175**, 417 (1955).
10. Y. Nakagawa, Proc. R. Soc. London, Ser. A **240**, 108 (1957).
11. F.H. Busse, R.M. Clever, Phys. Fluids **25**, 931 (1982).
12. Y. Nandukumar, P. Pal, EPL **112**, 24003 (2015).
13. W.M. Macek, M. Strumik, Phys. Rev. Lett. **112**, 074502 (2014).
14. A. Basak, R. Raveendran, K. Kumar, Phys. Rev. E **90**, 033002 (2014).
15. A. Basak, K. Kumar, Eur. Phys. J. B **88**, 1 (2015).
16. T. Yanagisawa, Y. Yamagishi, Y. Hamano, Y. Tasaka, M. Yoshida, K. Yano, Y. Takeda, Phys. Rev. E **82**, 016320 (2010).
17. T. Yanagisawa, Y. Hamano, T. Miyagoshi, Y. Yamagishi, Y. Tasaka, Y. Takeda, Phys. Rev. E **88**, 063020 (2013).
18. Y. Takeda, *Ultrasonic Doppler Velocity Profiler for Fluid Flow*, Vol. **101** (Springer Science & Business Media, 2012).
19. R. Moreau, *Magnetohydrodynamics* (Springer Science & Business Media, 1990).
20. M.J. Assael, I.J. Armyra, J. Brillo, S.V. Stankus, J. Wu, W.A. Wakeham, J. Phys. Chem. Ref. Data **41**, 033101 (2012).
21. G. Grötzbach, J. Comput. Phys. **49**, 241 (1983).
22. J. Magnaudet, M. Rivero, J. Fabre, J. Fluid Mech. **284**, 97 (1995).
23. S. Balay, S. Abhyankar, M.F. Adams, J. Brown, P. Brune, K. Buschelman, L. Dalcin, V. Eijkhout, W.D. Gropp, D. Kaushik, M.G. Knepley, L.C. McInnes, K. Rupp, B.F. Smith, S. Zampini, H. Zhang, PETSc users manual, Technical Report ANL-95/11 - Revision 3.6 (Argonne National Laboratory, 2015).
24. S.W. Morris, E. Bodenschatz, D.S. Cannell, G. Ahlers, Phys. Rev. Lett. **71**, 2026 (1993).